Flavor and topological current correlators in parity-invariant three-dimensional QED

Nikhil Karthik and Rajamani Narayanan

Phys. Rev. D **96**, 054509 — Published 11 September 2017

DOI: 10.1103/PhysRevD.96.054509

Flavor and topological current correlators in parity-invariant three-dimensional QED

Nikhil Karthik* and Rajamani Narayanan†

Department of Physics, Florida International University, Miami, FL 33199.

Abstract

We use lattice regularization to study the flow of the flavor-triplet fermion current central charge C_J^f from its free field value in the ultraviolet limit to its conformal value in the infrared limit of the parity-invariant three-dimensional QED with two flavors of two-component fermions. The dependence of C_J^f on the scale is weak with a tendency to be below the free field value at intermediate distances. Our numerical data suggests that the flavor-triplet fermion current and the topological current correlators become degenerate within numerical errors in the infra-red limit, thereby supporting an enhanced O(4) symmetry predicted by strong self-duality. Further, we demonstrate that fermion dynamics is necessary for the scale-invariant behavior of parity-invariant three-dimensional QED by showing that the pure gauge theory with non-compact gauge action has non-zero bilinear condensate.

PACS numbers: 11.15.Ha, 11.10.Kk, 11.30.Qc

*Electronic address: nkarthik@fiu.edu

†Electronic address: rajamani.narayanan@fiu.edu

I. INTRODUCTION

There is significant numerical evidence that parity invariant three dimensional QED, in addition to being asymptotically free, is scale-invariant in the infra-red for all even values of N, the number of flavors of massless two-component fermions [1, 2] [1]. In particular, it has been shown that the theory with $N = 2$ is consistent with a vanishing bilinear condensate using two different lattice regularization schemes. It is now important to characterize the infra-red fixed point for $N = 2$.

Denoting the two flavors of two-component fermions by $(\bar{\chi}_i, \chi_i)$, $i = 1, 2$, we define one of the flavor-triplet scalar and vector bilinear operators as

$$\Sigma(\mathbf{x}) = \bar{\chi}_1(\mathbf{x})\chi_1(\mathbf{x}) - \bar{\chi}_2(\mathbf{x})\chi_2(\mathbf{x}); \qquad V_k(\mathbf{x}) = \bar{\chi}_1(\mathbf{x})\sigma_k\chi_1(\mathbf{x}) - \bar{\chi}_2(\mathbf{x})\sigma_k\chi_2(\mathbf{x}), \tag{1}$$

where $\mathbf{x} = (x, y, t)$. In [2], we showed that both the correlators show massless behavior, and we provided some results concerning the scaling dimensions of these two operators. The scalar correlator gradually changes from the free field behavior of $|\mathbf{x}|^{-4}$ at short distances to $|\mathbf{x}|^{-2\Delta_\Sigma}$ at large distances and the scaling dimension was found to be $\Delta_\Sigma = 1.0 \pm 0.2$. This result is consistent with the one obtained in [4, 5] using an expansion in large number of flavors [2] and with our own estimate of the mass anomalous dimension from the finite size scaling of the low-lying eigenvalues of the Dirac operator. The power-law decay of the flavor-triplet vector correlator remains $|\mathbf{x}|^{-4}$ at all distances since it is a conserved current. Since, we project correlators to zero spatial momentum to study them as a function of the Euclidean time separation t, the vector correlator decays as t^{-2} and the coefficient, $C_J^f(t)$, of this power-law decay [3] is what we refer to as the amplitude, and it becomes the flavor current central charge at the conformal point in the infra-red limit $t \to \infty$.

In this paper, we extend our results further in the following three ways:

1. Assuming conformal symmetry that is valid for large number of flavors and using a diagrammatic approach [6, 7], the amplitude of the correlator of the vector bilinear is found to be
$$\frac{C_J^f(t \to \infty)}{C_J^f(t \to 0)} = 1 + \frac{0.1429}{N} + \mathcal{O}\left(\frac{1}{N^2}\right). \tag{2}$$

[1] An earlier lattice calculation [3] using staggered fermions provides evidence for the absence of bilinear condensate for $N \geq 4$.

[2] Care should be used in taking this agreement at face value since an agreement is found by setting the number of flavors to two in their computation which need not be large.

[3] Since we are interested in ratios of C_J^f, any difference by a factor in our definition of C_J^f from elsewhere in the literature is inconsequential.

Thus, in the infra-red limit the value of C_J^f is larger the the free field value in the ultraviolet by a factor 1.07 for $N = 2$. Numerical conformal bootstrap [8] has been used to obtain the allowed region for this amplitude directly for two flavors. In this work, we study the behavior of $C_J^f(t)$. For the values of t where a reliable numerical estimate is possible our value lies close to its ultraviolet value. However, we find that $C_J(t)$ has a tendency to flow from its ultraviolet value at small t to a value below it at intermediate values of t. If it has to agree with the result from the diagrammatic approach in Eq. (2), the flow has to be non-monotonic, and our result does not strongly support it.

2. A self-duality has been proposed to be valid at the infra-red fixed point of $N = 2$ two component QED [9–12]. Since the topological current on one side of the duality maps onto the flavor-triplet vector current on other side of the duality, their correlators have to be degenerate at large separations. This also implies that the amplitude of the correlator of the vector bilinear C_J^f and the amplitude of the topological current correlator C_J^t have to be the same. This SU(2)× SU(2) symmetry becomes an emergent O(4) symmetry [12]. We provide evidence in favor of this argument. This would imply that the infra-red fixed point in QED_3 coupled to small number of fermion flavors is qualitatively different from the one expected in large N.

3. Unlike the theory with two flavors of two component fermions, quenched QED (limit where the number of flavors is taken to zero) has a non-zero bilinear condensate. This can be considered as a follow-up of a calculation [13] done three decades ago when computational power was not sufficient to extract the continuum value of the condensate. Thus, the fermions used as a probe in pure gauge theory develops a scale, and fermion dynamics is necessary for a scale-invariant behavior.

II. FLOW OF C_J^f FROM THE ULTRAVIOLET TO THE INFRARED

Using the fact that QED_3 is a super-renormalizable theory, we write the lattice coupling appearing in the non-compact gauge action on a L^3 periodic lattice as $\beta = 2L/\ell$, where ℓ is the physical extent of the three-dimensional torus and the continuum limit is obtained by $L \to \infty$. The details of the simulation for $N = 2$ QED_3 using massless overlap fermions are given in [2]. We analyzed the data at $L = 12, 14, 16, 20, 24$ and $\ell = 4, 8, 16, 24, 32, 48, 64, 96, 112, 128, 144, 160, 200$. In order to improve the signal, we project the correlators to zero momentum in spatial directions. The zero spatial momentum projected

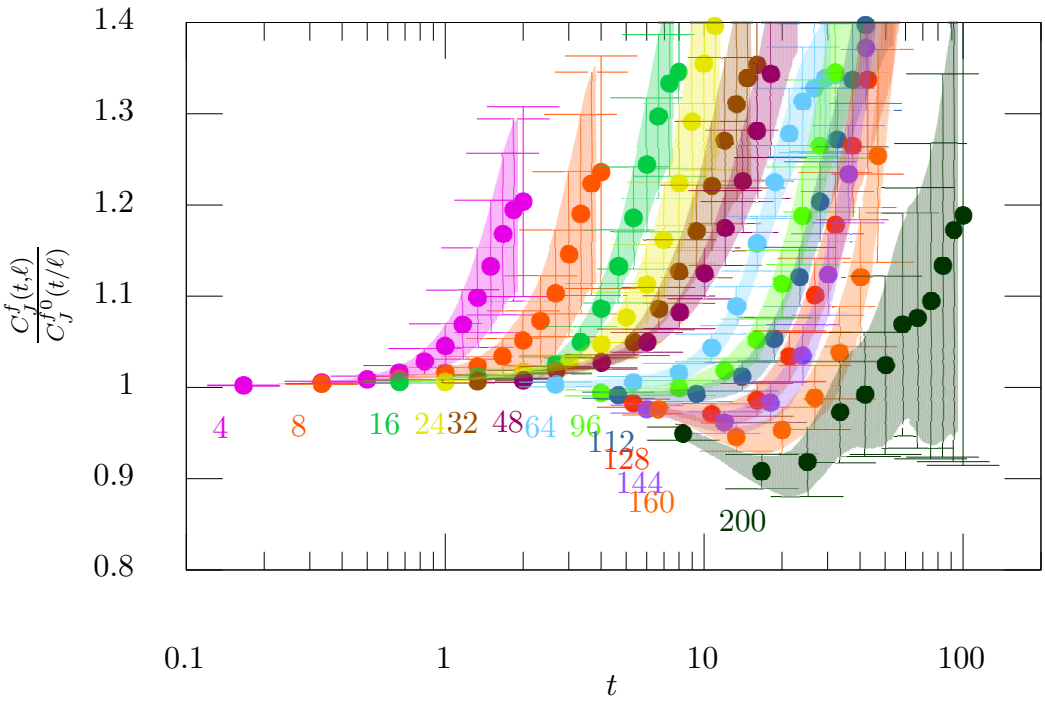

FIG. 1: The data for $\frac{C_J^f(t,\ell)}{C_J^{f0}(t/\ell)}$ from different ℓ is put together as a function of t. All the correlators in the figure were determined on finite lattice $L = 24$. The 1-σ error bands interpolating the data points are also shown.

flavor-triplet vector correlator determined at finite physical volume is

$$G_V(t,\ell) = \int dx\ dy\ \left\langle \sum_{k=1}^{2} V_k(0,0,0) V_k(x,y,t) \right\rangle \equiv \frac{C_J^f(t,\ell)}{t^2}. \tag{3}$$

The corresponding expression on the lattice in terms of the overlap fermion propagators is given in [2]. In order to study the flow of C_J^f from UV to IR, we study the ratio $C_J^f(t,\ell)$ in the interacting theory to the free field value $C_J^{f0}\left(\frac{t}{\ell}\right)$ obtained on the same L^3 lattices *i.e.*,

$$\frac{C_J^f(t,\ell)}{C_J^{f0}(\frac{t}{\ell})} = \frac{G_V(t,\ell)}{G_V^{\rm free}(\frac{t}{\ell})}, \tag{4}$$

where $G_V^{\rm free}$ is the correlator obtained by putting all lattice gauge fields to zero.

In order to obtain the ratio $\frac{C_J^f}{C_J^{f0}}$ in the continuum limit as well as in the infinite volume limit, one has to take the $L \to \infty$ limit of the ratio at different t at fixed ℓ, and then take the $\ell \to \infty$ limit at fixed t. Before we incorporate this procedure, we put together the data for the ratio from different ℓ at $L = 24$ as a function of t in Figure 1. At finite L and ℓ, we only obtain values for $G_V\,(t,\ell)$ at certain discrete values $t = T\frac{\ell}{L}$ where $T = 1, \ldots, \frac{L}{2}$ — these are the solid

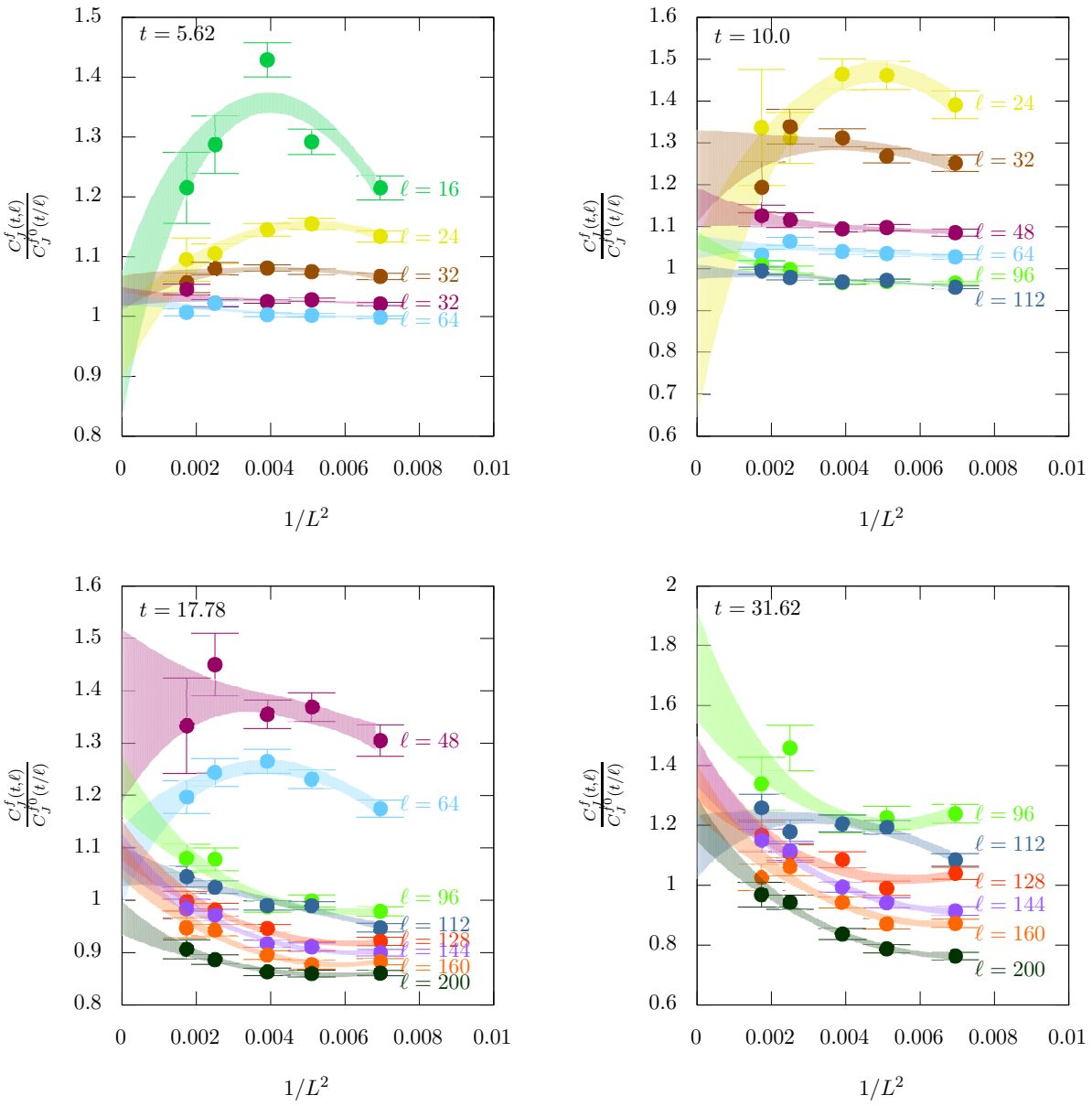

FIG. 2: Continuum limits, $\lim_{L\to\infty} \frac{C_J^f(t,\ell)}{C_J^{f0}(t/\ell)}$ at various ℓ (differentiated by the colors in each panel) at the same values of t using $L = 12, 14, 16, 20$ and 24. The four panels correspond to different t. The continuum extrapolation is using a $A + B/L^2 + C/L^3$ fit to the data. The 1-σ error bands for the extrapolation are shown along with the data.

circles in Figure 1, with each color corresponding to data from different ℓ. We can qualitative see the following. At small t, the value of $\frac{C_J^f}{C_J^{f0}}$ is almost unity as expected. However, at any larger fixed value of t, the value of the ratio decreases with ℓ and goes below unity for certain intermediate t.

Now we proceed to take care of the finite lattice spacing and the finite volume effects in the

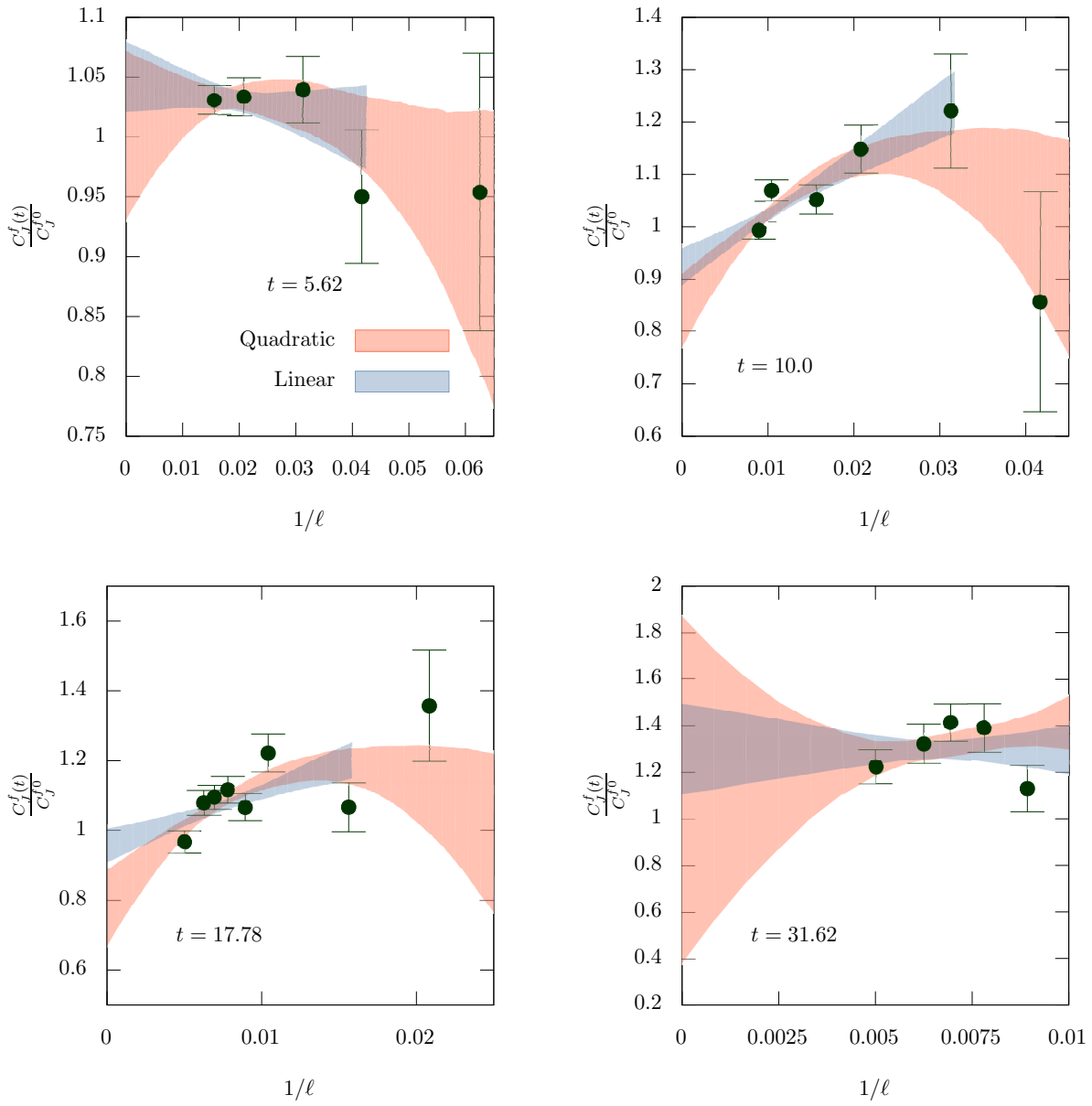

FIG. 3: Infinite volume limits, $\lim_{\ell\to\infty} \frac{C_J^f(t,\ell)}{C_J^{f0}(t/\ell)}$, at different fixed values t are shown in the four panels. The black circles are the values obtained in the continuum limit (refer Figure 2) at different ℓ at a value of t. The 1-σ error band for $\frac{C_J^f}{C_J^{f0}}(t) + \frac{k_1}{\ell}$ extrapolation is shown in red. The 1-σ error band for $\frac{C_J^f}{C_J^{f0}}(t) + \frac{k_1}{\ell} + \frac{k_2}{\ell^2}$ extrapolation is shown in blue.

data. First, we interpolate our data between the discrete values of $t = T\frac{\ell}{L}$ using cubic spline. This is justified since the data for the ratio is smooth and regular as seen in Figure 1. The error bars on the interpolation is obtained by bootstrap. The 1-σ error band for the interpolation is shown along with the data in Figure 1. This gives us results in the range $t \in [\frac{\ell}{L}, \frac{\ell}{2}]$. In Figure 2, we address the lattice spacing effects. Each panel corresponds to a fixed value of t.

Given that we wish to use data at all five values of L to obtain the continuum limit, we can only use ℓ ranging from $2t$ to $12t$ at a given t. These are the different colored symbols in each panel in Figure 2. Since we have used fermions with exact flavor symmetry on the lattice, the leading lattice correction is $\mathcal{O}\left(\frac{1}{L^2}\right)$, and we include $\frac{1}{L^2}$ and $\frac{1}{L^3}$ corrections to extrapolate to the continuum limit $L \to \infty$. These extrapolations are shown by the error bands in Figure 2.

Using the continuum limits so obtained for $\frac{C_J^f(t,\ell)}{C_J^{f0}\left(\frac{t}{\ell}\right)}$, we show its ℓ dependence at various t in the four panels of Figure 3. We were able to capture the ℓ dependence by a linear, $\frac{C_J^f}{C_J^{f0}}(t,\ell) = \frac{C_J^f}{C_J^{f0}}(t) + \frac{k_1}{\ell}$, dependence in the range of t we explored. This is shown as the blue 1-σ error band in the different panels. However, to address systematic effects of the fit, we also use a quadratic fit, $\frac{C_J^f}{C_J^{f0}}(t,\ell) = \frac{C_J^f}{C_J^{f0}}(t) + \frac{k_1}{\ell} + \frac{k_2}{\ell^2}$, to extrapolate to $\ell \to \infty$. This is shown as the red 1-σ error bands in the panels. At smaller t, the errors are smaller and hence the errors on the extrapolations are controlled. In fact for $t < 6$, only a weak dependence on ℓ is seen and one can drop any $1/\ell$ dependence, and the values are consistent with 1. But there exists a range of t ($t = 10.0$ falls in this range) where this quantity has a value less than unity. This does not violate the requirement of monotonic decrease of the propagator with t since it only implies the relation

$$\frac{d \ln C_J^f(t,\infty)}{dt} < \frac{2}{t}. \tag{5}$$

But it suggests that $C_J^f(t, \ell \to \infty)$ cannot be a monotonic function of t if it has to be consistent with Eq. (2). However, as t is increased the errors increase, and hence we lose our ability to determine the infinite volume limit for $t > 30$.

The flow of $C_J^f(t)$ in infinite physical volume from its ultraviolet value normalized to unity toward its infrared value is shown in Figure 4. The top panel shows the result obtained using a linear extrapolation in $1/\ell$ to the infinite volume limit at fixed values of t. The darker band shows the 68% confidence interval, while the lighter band encloses 95% confidence interval. We see that the flow either remains at the ultraviolet value or it increases slightly first from its value in the ultraviolet limit. In the same panel, the infinite volume limits at $t < 6$ obtained assuming no ℓ dependence in the data is shown as the light blue band. It is even more evident that $C_J^f(t)$ approaches the free field value in the ultraviolet limit. There is an intermediate region in t (around $t = 10$) where there is evidence that it is below its value in the ultraviolet limit. The bottom panel of Figure 4 compares the estimate of the flow when both $1/\ell$ and $1/\ell^2$ terms are used to estimate the value at infinite volume. We see that relevant qualitative aspects of the flow are not affected by the choice of the fit. In particular, the inclusion of higher order corrections in $\frac{1}{\ell}$ suggests that the flow remains below free field value even beyond the

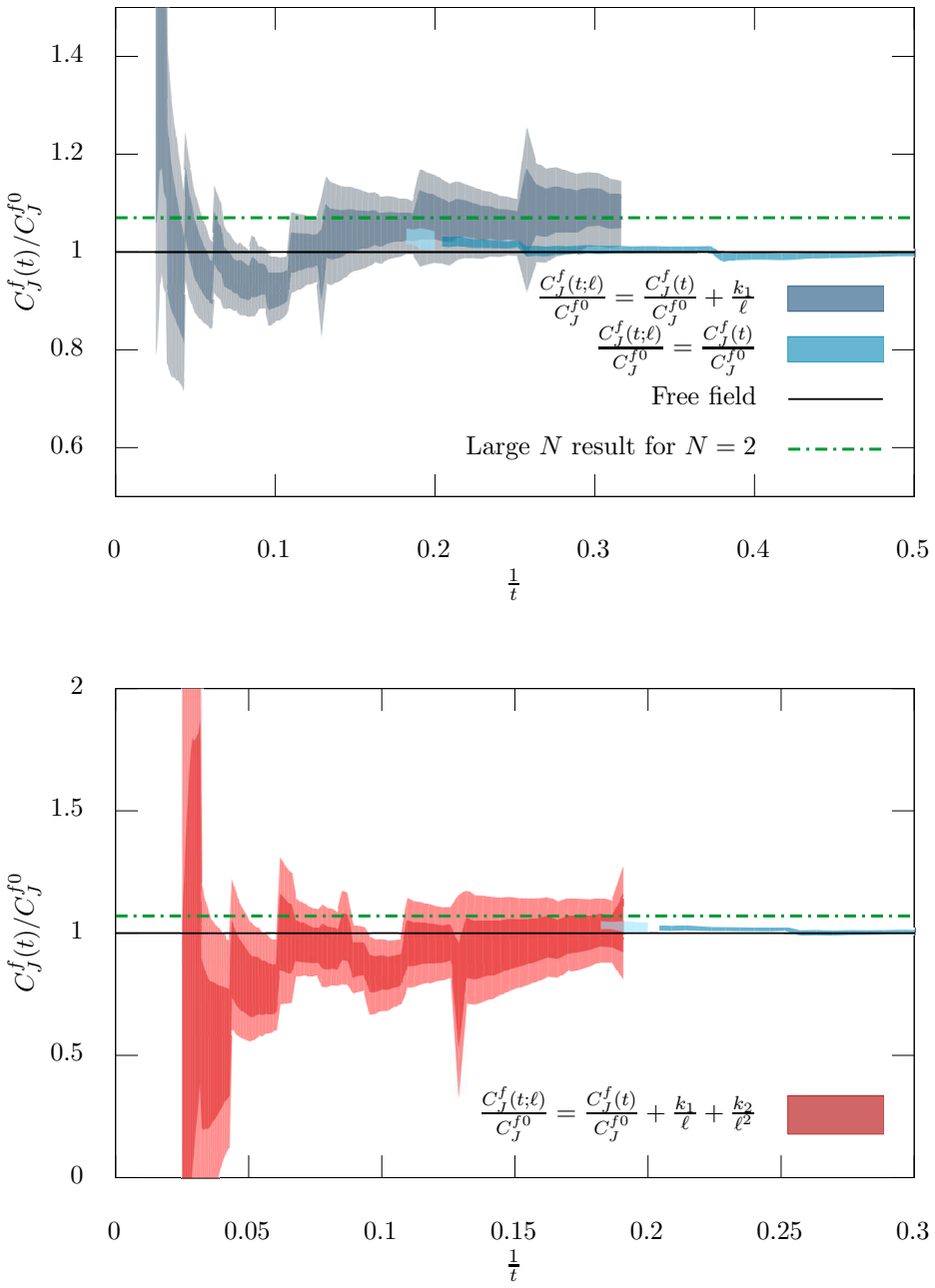

FIG. 4: Flow of $\frac{C_J^f(t)}{C_J^{f0}}$ from the UV to the IR fixed point. The top and the bottom panels differ by the fits used for the $\ell \to \infty$ extrapolation; the top panel includes only the $1/\ell$ effect (as shown by the blue bands in Figure 3) while the bottom panel includes $1/\ell$ as well as $1/\ell^2$ effects (as shown by red bands in Figure 3). The darker band is the 68% confidence interval and the lighter band is the 95% confidence interval. In both the top and the bottom panels, the blue thin band that remains very close to 1 for $1/t > 0.2$ is obtained assuming no finite ℓ effects while taking the $\ell \to \infty$ limit at those t. The black line is the free field value in the ultraviolet $1/t \to \infty$ limit while the green dotted line is expectation in the infrared $1/t \to 0$ limit from a large N computation.

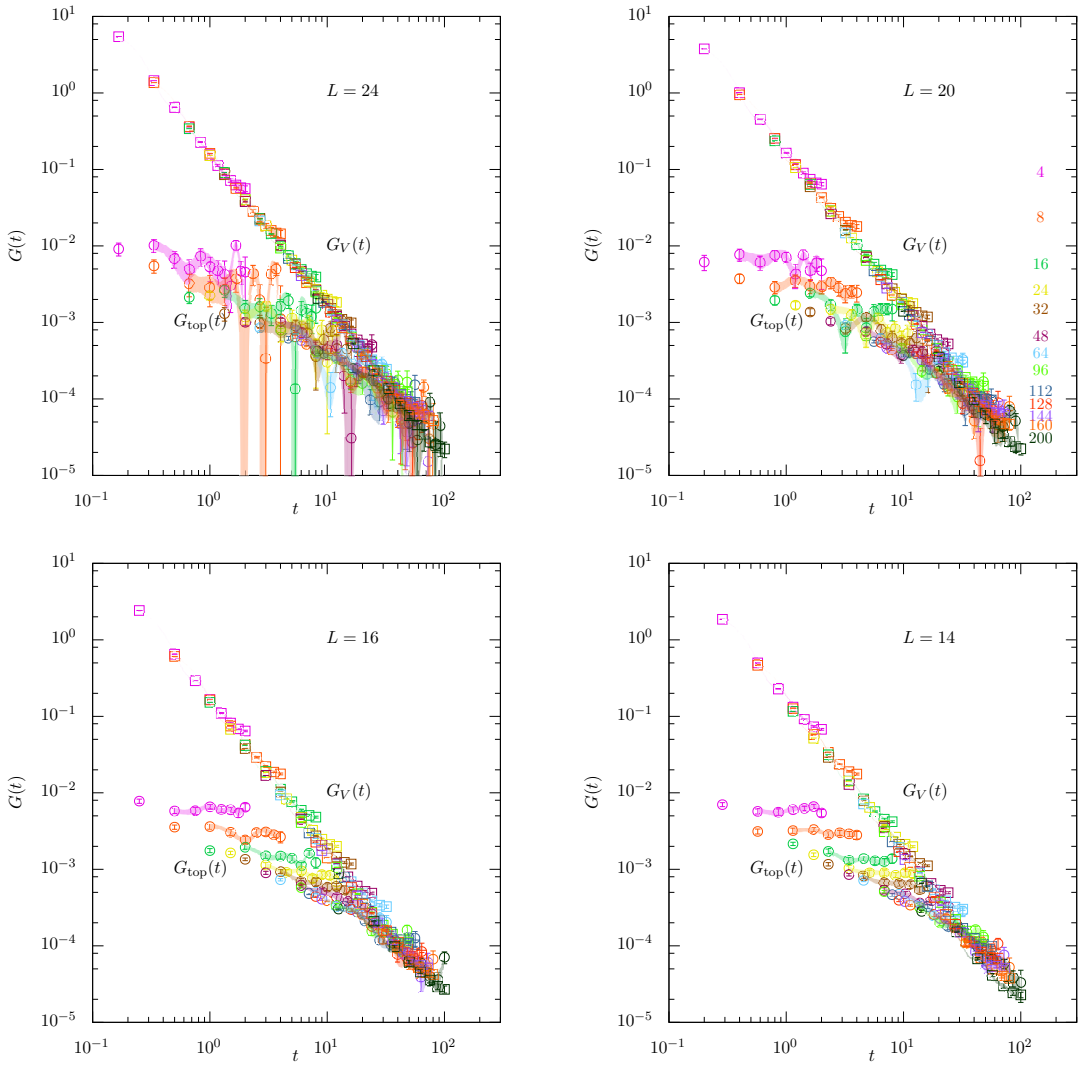

FIG. 5: The vector correlator $G^V(t)$ (squares) and the topological current correlator $G_{\rm top}(t)$ (circles) at different fixed L are shown in the four panels. The different colored symbols at each L correspond to the data from different ℓ as specified by the color-code in the top-right panel.

intermediate region in t. If this trend continues at even larger t closer to the infra-red limit, it would be inconsistent with Eq. (2), but that is a result valid for large number of flavors. An analytic calculation at finite N for the flow of C_J^f near the infra-red fixed point (*i.e.*, large but finite t) would enable an extrapolation of our result, reliable at finite t, to $t \to \infty$.

III. ENHANCED O(4) SYMMETRY

Arguments based on the self-duality of the two flavor massless QED_3 suggests that the global SU(2) symmetry present in QED_3 Lagrangian gets enhanced into O(4) symmetry at the

conformal point in the infra-red limit [12]. If this is true, the amplitude of the correlator $G_{\rm top}(t)$ of the topological current,

$$j_k(\mathbf{x}) = \frac{1}{2\pi}\epsilon_{klm}\partial_l A_m(\mathbf{x}), \qquad G_{\rm top}(t) = \int dxdy \left\langle \sum_{k=1}^{2} j_k(0,0,0) j_k(x,y,t) \right\rangle, \tag{6}$$

has an asymptotic behavior given by [4]

$$G_{\rm top}(t) = \frac{C_J^t(t=\infty)}{t^2}; \qquad \text{as} \quad t \to \infty, \tag{7}$$

and we expect

$$C_J^t(t=\infty) = C_J^f(t=\infty). \tag{8}$$

This is a non-trivial check since this correlator is trivial in the pure gauge theory where there is no dependence on the separation t. However, the computation using Feynman diagrams for QED_3 with a large number of flavors [7] yields [5]

$$\frac{C_J^t(\infty)}{C_J^f(0)} = \frac{3.3423}{N} - \frac{0.4634}{N^2} + \mathcal{O}\left(\frac{1}{N^3}\right). \tag{9}$$

For $N = 2$, the value is 1.55. This result is mildly different from the value 1.07 from Eq. (2) implying that the large N calculation does not predict enhanced O(4) symmetry for $N = 2$. This is not surprising since Eq. (9) is strictly valid only for large N and the equality of the two amplitudes is expected only for $N = 2$.

On the lattice, we determined the topological current correlator as

$$\begin{aligned} j_k^{\rm lat}(T) &= \frac{1}{2\pi} \sum_{X,Y=1}^{L} \sum_{l,m} \epsilon_{klm} \left(\theta_m(\mathbf{X} + \hat{l}) - \theta_m(\mathbf{X}) \right); \\ G_{\rm top}(T) &= \frac{1}{\ell^2} \left\langle \sum_{k=1}^{2} j_k^{\rm lat}(T) j_k^{\rm lat}(0) \right\rangle \end{aligned} \tag{10}$$

where $\theta_k(\mathbf{X}) = A_k(\mathbf{X})\ell/L$ is the (unsmeared) lattice gauge field from the lattice site $\mathbf{X} = (X, Y, T)$. Also, we have projected j_k to zero momentum at both the source and sink time-slices in order to improve the signal, and then divided by $1/\ell^2$ to obtain the topological current correlator at zero spatial momentum. We do not use j_3 in the analysis since its integral over the xy-plane is zero for the non-compact gauge field we use. Also, the definition in the second line of Eq. (10) is consistent with the definition of the flavor-triplet vector bilinear correlator in Eq. (3).

---

[4] The scaling dimension of this operator is same as the vector bilinear [14].

[5] Note that the normalization of the vector current and the topological current differ by a factor of 2 in [7, 15] but we have normalized both currents by $C_J(0)$.

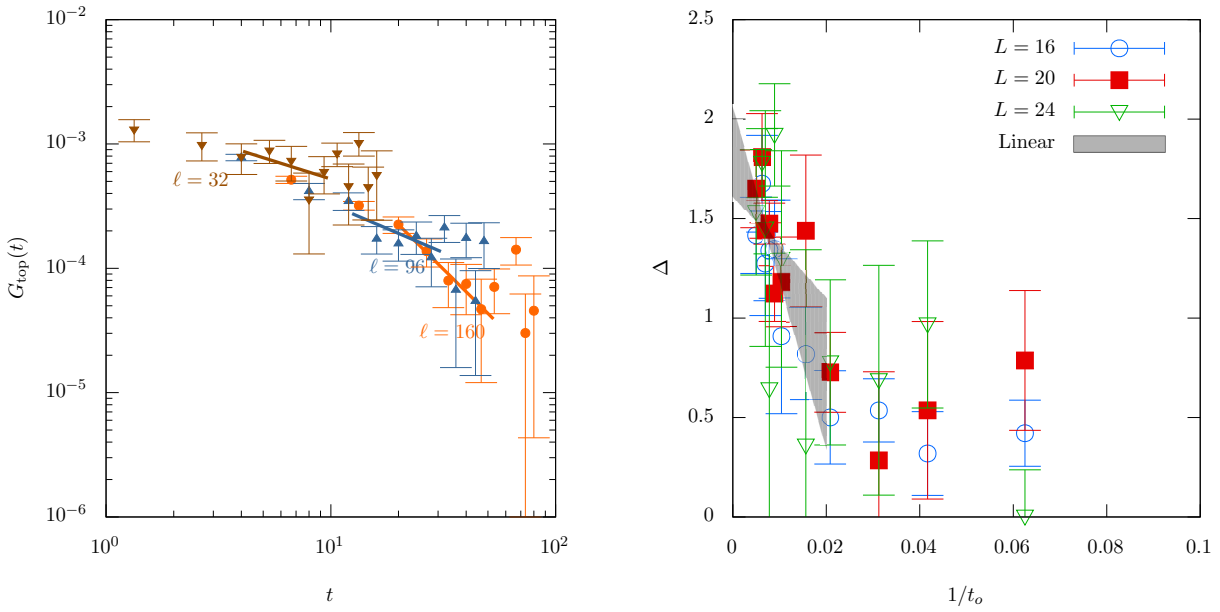

FIG. 6: (Left) Power-law fits $G_{\rm top}(t) \sim t^{-\Delta}$, shown as solid straight lines, using data in the range $t_o \le t \le 2t_o$. The different colored symbols correspond to $G_{\rm top}(t, \ell)$ from different ℓ. We chose $t_o = \ell/8$. (Right) The increase of the exponent Δ towards the value 2 as t_o becomes larger is shown. The different colored symbols correspond to different lattice sizes L. The gray band is a linear $A+B/t_o$ fit to the $L = 20$ data.

The results for $G_{\rm top}(t)$ are compared with $G_V(t)$ in Figure 5. We have used the data from different ℓ at same L in order to span a range of t, as explained in the last section. The different colored symbols in each of the four panels in Figure 5 correspond to different ℓ. A detailed analysis of the type performed in the previous section does not work here due to larger errors in the topological current correlator, which is a pure-gauge observable, compared to the fermionic vector current correlator. This lead to uncontrolled errors when we attempted the $L \to \infty$ and $\ell \to \infty$ extrapolations, especially at large values of t where we are interested. Therefore, we restrict ourselves to comparisons on finite lattices at different ℓ.

Unlike $G_V(t)$ which is a correlator of a conserved current, the behavior of $G_{\rm top}(t)$ is not a simple power law for all values of t. At small values of t, $G_{\rm top}(t)$ is orders of magnitude smaller than that of $G_V(t)$. The propagator has to be monotonic in t and if it were to have a non-zero limit for every t as $\ell \to \infty$, then our data suggests that the propagator approaches a non-zero constant at these short distances. [6] As t becomes larger ($t > 10$), $G_{\rm top}$ is seen to approach

[6] We cannot rule out the possibility that this propagator has a trivial $\ell \to \infty$ limit for all t. We assume this is not the case.

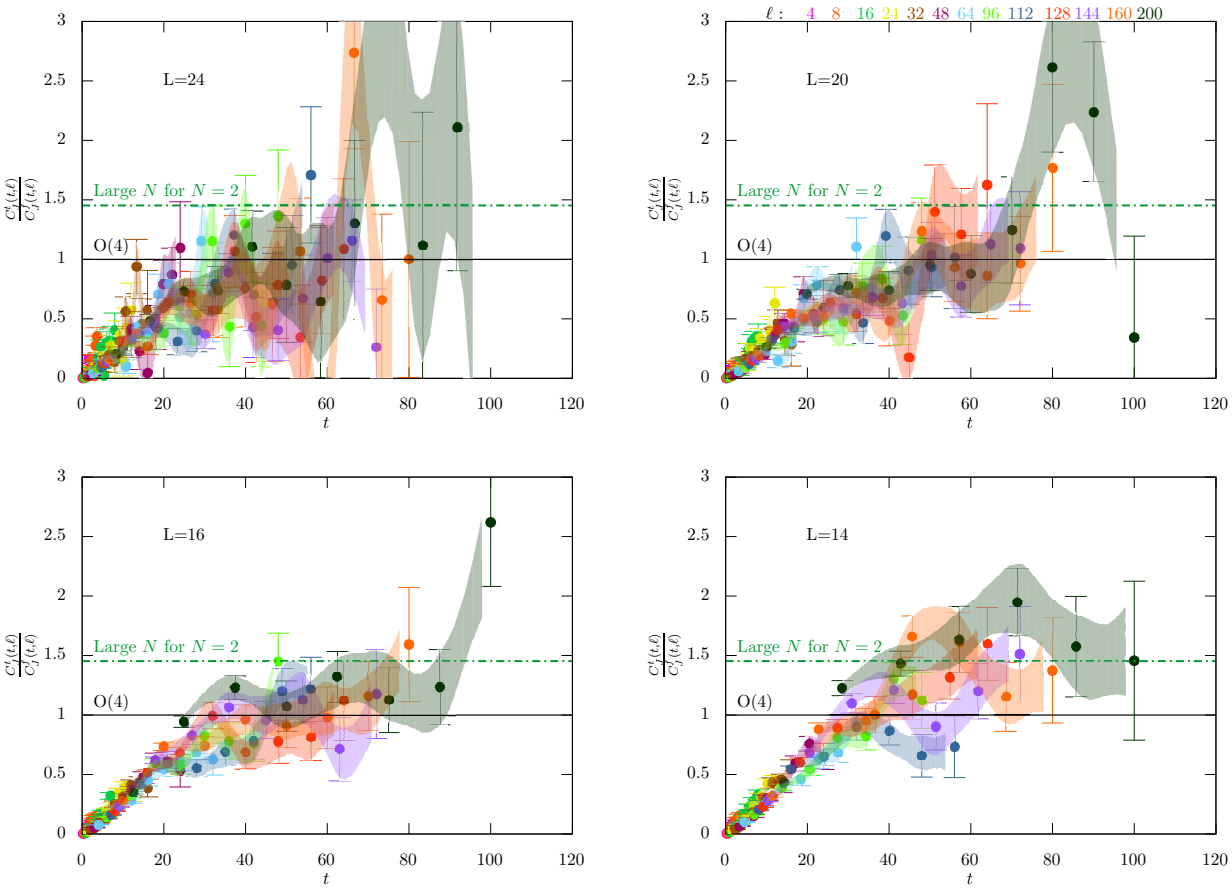

FIG. 7: The ratio $\frac{C_J^t(t,\ell)}{C_J^f(t,\ell)}$ are shown as a function of t at different fixed L in the four panels. The different colored symbols and bands are the data and their cubic spline interpolations at different ℓ. The color code for ℓ is shown on top of the top-right panel. The expectation for this ratio from the O(4) symmetry is 1 as $t \to \infty$. The dot-dashed line is the result from the large-N computation extended to $N = 2$.

G_V. Our data at all values of L show reasonably good evidence for a region in t where the correlators $G_V(t)$ and $G_{\rm top}(t)$ match. The errors in $G_{\rm top}$ get worse as L increases due to a decrease in statistics associated with an increase in autocorrelation in the simulation when L is increased.

The degeneracy of the current correlators requires that $G_{\rm top}(t) \sim t^{-2}$ for large t. To verify this, we fit a power-law $G_{\rm top}(t,\ell) \sim t^{-\Delta}$ to the correlators determined in finite physical volume ℓ^3, using data that lie in a range $t_o \le t \le 2t_o$. We find a reasonable power-law behavior when we choose the range corresponding to $t_o = \ell/8$ — a reason could be that the finite volume effects at $t \approx \ell/2$ are avoided, and finite L effects at even smaller t/ℓ are also avoided. Such sample power law fits for the correlators at $\ell = 32, 96$ and 160 on $L = 24$ lattice are shown in the left panel of Figure 6. On the right panel of Figure 6, we show the exponent $\Delta(t_o)$ so

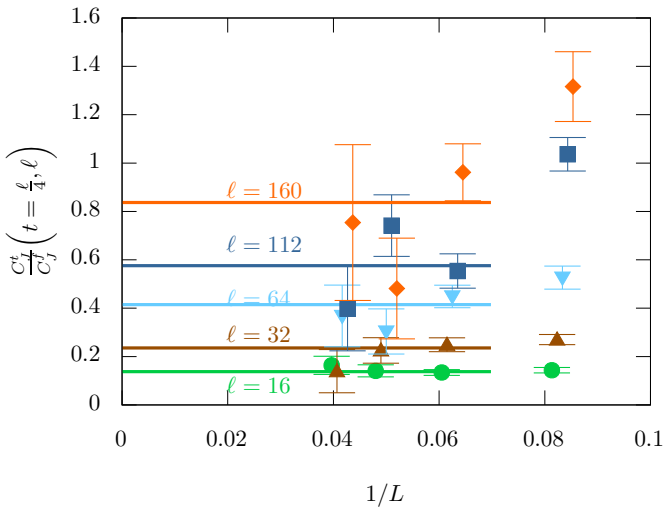

FIG. 8: Lattice spacing effects in $\frac{C_J^t}{C_J^f}$ at $t = \ell/4$ data point as determined using correlators at different ℓ. The values at $L = 16, 20$ and 24 seem consistent within error bars. However, at larger ℓ at finite L, the error bars on the data also get larger to mask lattice spacing effects.

determined, as a function of $1/t_o$ at three different lattice sizes $L = 16, 20$ and 24. There is evidence at all three L that Δ approaches the expected value 2 in the $t_o \to \infty$ limit.

To further explore the comparative behavior of $G_V(t)$ and $G_{\rm top}(t)$ at large t, we have plotted their ratio

$$\frac{C_J^t(t,\ell)}{C_J^f(t,\ell)} \equiv \frac{G_{\rm top}(t,\ell)}{G_V(t,\ell)}, \tag{11}$$

in Figure 7 at four different L shown in the four panels. We have shown the ratio obtained from Eq. (2) and Eq. (9) for comparison. Within errors, the results at all values of L are consistent with the ratio approaching unity for larger t and we see no significant difference between $L = 16, 20, 24$ data. While one cannot use the $L = 14$ data at $t > 40$ to distinguish between the large N and O(4) cases, the results on finer $L = 16, 20, 24$ lattices seem to be more consistent at the level of 1-σ with the O(4) expectation. For $t > 60$, the data becomes very noisy. We illustrate the lattice spacing effects further in Figure 8 — we show $\frac{C_J^t(t,\ell)}{C_J^f(t,\ell)}$ as determined at $t = \ell/4$ [7] from the correlators determined in boxes of finite physical extents ℓ, as a function of $1/L$. The $L = 16, 20$ and 24 data are always consistent with each other as seen by the horizontal straight lines in the figure. Any increase in finite lattice spacing effect as ℓ is increased at finite L is overcome by a corresponding increase in the noise in the topological

[7] In this way, interpolation can be avoided as the data point at $t = \ell/4$ is always present on $L = 12, 16, 20$ and 24.

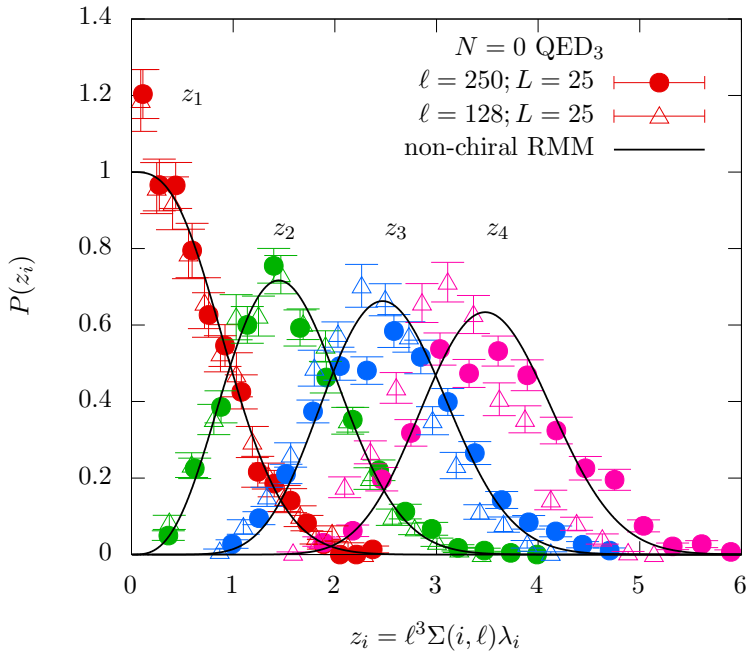

FIG. 9: Distribution of the low-lying eigenvalues, λ_i for $i = 1, 2, 3, 4$, of the overlap Dirac operator (data points) scaled by ℓ^3. The distributions are also multiplied by constants $\Sigma(i, \ell, L)$ such that their means match that of the corresponding distributions of the low-lying eigenvalues from the non-chiral random matrix model with $N = 0$ (solid black curves). Further, in the $\ell \to \infty$, all the $\Sigma(i, \ell, L)$ have to approach the same value independent of i.

current correlator. Therefore, at the level of statistical uncertainties in Figure 7, the lattice spacing effects seem to be unimportant.

IV. QUENCHED ($N = 0$) QED$_3$

Unlike QED$_3$ with dynamical fermions, we expect the quenched theory where the fermions are used as a probe to have a non-conformal infra-red behavior with a scale set by the gauge coupling. We will assume a non-compact action for the gauge field and therefore monopoles will be suppressed. As in our previous paper [2], we study the low lying microscopic eigenvalues, $i\lambda_j$, of the anti-Hermitian massless overlap Dirac operator. The presence of a bilinear condensate implies a non-zero density at zero eigenvalue and level repulsion implies that the level spacing of eigenvalues near zero will be inversely proportional to ℓ^3. The individual distributions of the low-lying eigenvalues (ordered by their absolute values) will be governed by an appropriate non-chiral random matrix model (RMM) [16, 17], which in our case will be a Hermitian random matrix model.

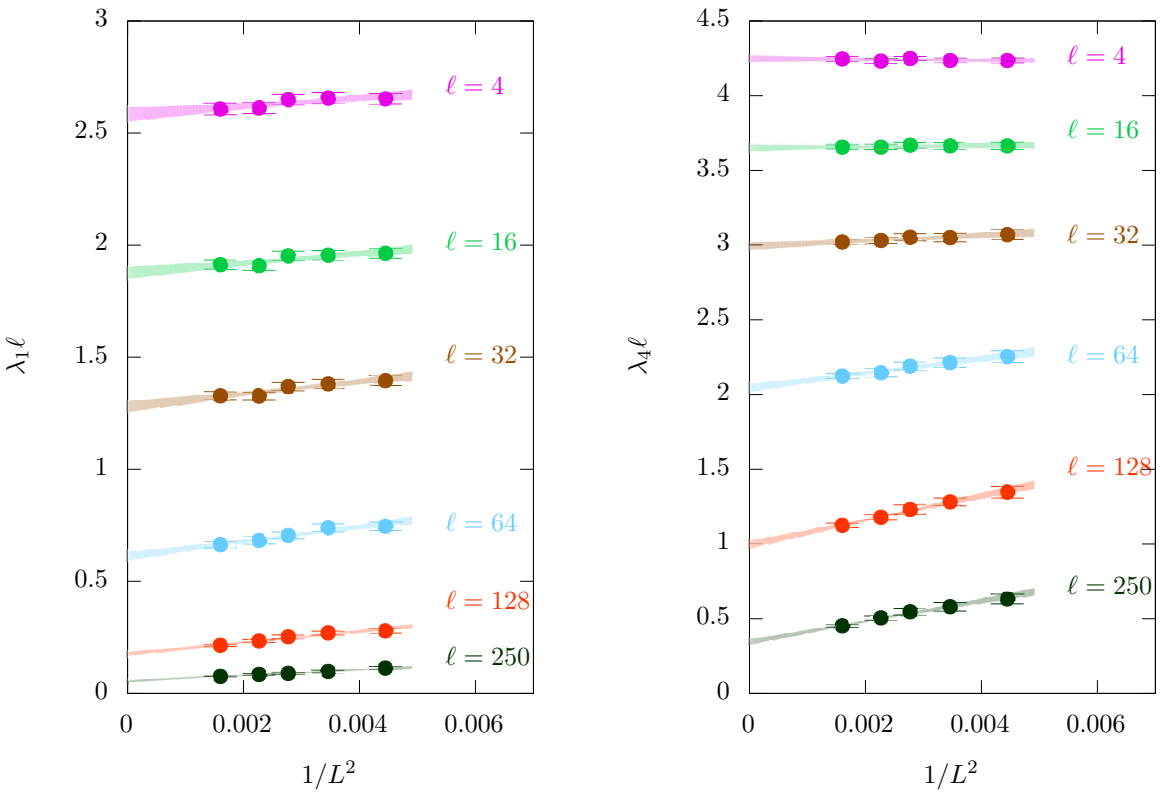

FIG. 10: Continuum extrapolation of first (left panel) and the fourth (right panel) smallest eigenvalues of the overlap Dirac operator. The points of different colors are the data at different fixed ℓ. The bands are the $1/L^2$ extrapolation of the data.

We simulated the quenched $N = 0$ QED$_3$ by Monte Carlo sampling of the Fourier modes of the gauge field. We used lattices with $L = 15, 17, 19, 21$ and 25 in order to take the continuum limit at different ℓ. On the random matrix side, the distributions of the low lying eigenvalues z_j in the RMM model can be obtained by using the sinc-kernel and the associated Fredholm determinants [18, 19]. We numerically evaluated the eigenvalues of the kernel required for the computation of the determinants and traces of the resolvents, and we were able to determine the distributions of the five lowest eigenvalues z_j in the RMM needed for our comparison to a very good accuracy.

The bilinear condensate, if present, can be obtained by matching the distribution of the low-lying microscopic eigenvalues in the pure gauge theory to that from the RMM model. In Figure 9, we make such a comparison by scaling $\lambda_i(\ell, L)$ by a constant $\Sigma(i, \ell, L)\ell^3$ such that the means of the two distributions match *i.e.*,

$$\Sigma(i, \ell, L) = \frac{\langle z_i \rangle}{\langle \lambda_i(\ell, L) \rangle \, \ell^3}. \tag{12}$$

A good agreement is seen between the distributions till the 4th eigenvalue just by this simple

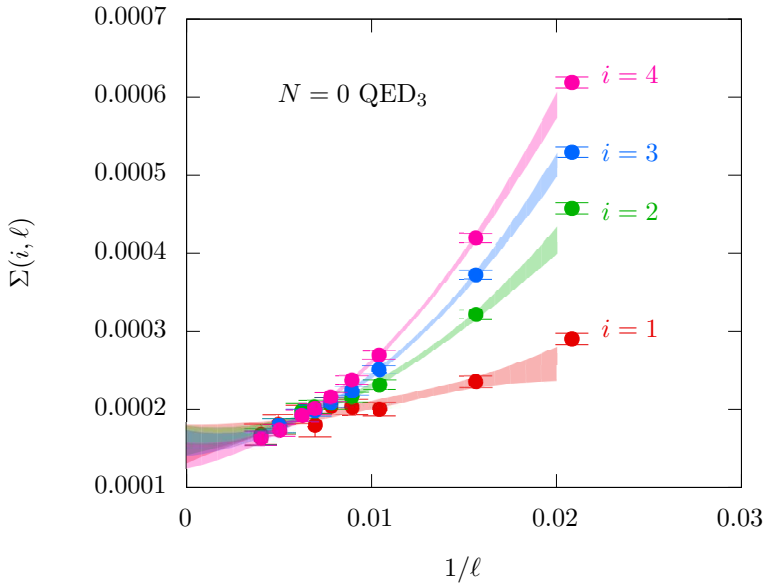

FIG. 11: The infinite ℓ limit of the condensate $\Sigma_i(i,\ell) = \frac{\langle z_i \rangle}{(\langle \lambda_i(\ell) \rangle \ell^3}$, where $\langle \lambda_i(\ell) \rangle$ is the i-th eigenvalue of the overlap Dirac operator after taking the $L \to \infty$ continuum limit, and the z_i's are the eigenvalues of the non-chiral RMM. The 1-σ bands for an $A + B/\ell + C/\ell^2$ extrapolation of the finite volume data are shown. Agreement between different $\Sigma(i, \ell = \infty)$ are seen, thereby ensuring the self-consistency of the random matrix analysis. We estimate the condensate to be $\Sigma = 1.5(1) \times 10^{-4}$.

scaling. The agreement gets better as ℓ is increased as expected when a condensate is present. In the $\ell \to \infty$ limit, taken after the $L \to \infty$ continuum limit, the values of Σ obtained from the different microscopic eigenvalues have to be the same, and it is the value of the condensate. We now proceed to show this to be the case and obtain the value of Σ.

We extrapolate $\langle \lambda_i(\ell, L) \rangle \ell$ to the continuum by using a fit of the form $\langle \lambda_i(\ell, L) \rangle = \langle \lambda_i(\ell) \rangle \, \ell + k/L^2$ at each fixed finite box size ℓ. We show this extrapolation at different ℓ for the first and the fourth smallest eigenvalues on the left and right panels of Figure 10 respectively. Using these continuum extrapolated values of $\langle \lambda_i(\ell) \rangle \ell$, we determined the values of $\Sigma(i, \ell)$ from Eq. (12). The dependence of $\Sigma(i, \ell)$ on ℓ for the first four eigenvalues are shown in Figure 11. A strong dependence on ℓ is seen. However, one can easily see that they approach a non-zero limit as $\ell \to \infty$. We extract this limit from different ith eigenvalues from a $\Sigma(i, \ell) = \Sigma(i) + a_1/\ell + a_2/\ell^2$ extrapolation using the data at $\ell \geq 64$. The value of the condensate for i =1,2,3 and 4 are $1.5(2) \times 10^{-4}$, $1.6(2) \times 10^{-4}$, $1.6(2) \times 10^{-4}$ and $1.4(2) \times 10^{-4}$ respectively. They are all consistent with each other thereby assuring the consistency of the method. Taking their average, we estimate the value of the condensate in quenched QED$_3$ to be $1.5(1) \times 10^{-4}$. For comparison, the value of the condensate per color degree of freedom in the 't Hooft limit is $4.2(4) \times 10^{-3}$ [20].

V. CONCLUSIONS

A further study of the correlator of the flavor-triplet vector bilinear in QED_3 with two flavors of two component massless fermions suggests an enhanced O(4) symmetry in the infra-red limit as predicted by a strong duality [12]. The amplitude of the correlator of the flavor-triplet vector bilinear C_J^f and the amplitude of the correlator of the topological current C_J^t are the same in the large distance limit in our numerical calculation. There is an intermediate region in the separation where the amplitude C_J^f itself is lower than its ultraviolet value and it is likely that this trend remains as one approaches the infrared limit. A further check on whether the enhanced O(4) symmetry in $N = 2$ QED_3 also implies its duality to the easy plane $NCCP^1$ model proposed in [12] will involve a computation of the scaling dimensions of certain four Fermi operators. We plan to address this along with the behavior of other higher dimensional composite operators in the future.

We show clear evidence for a bilinear condensate in the quenched theory – pure gauge theory with massless fermions as a probe. Our results also show that the quenched theory has a finite condensate in the infinite volume limit. This is contrary to what happens in even dimensions [21, 22] where a diverging condensate is usually associated with the presence of an axial anomaly in the theory. We have studied the pure gauge theory where contributions from monopoles have been suppressed. It would be interesting to see if the condensate would diverge in a theory with a compact gauge action. Compact gauge action poses a technical problem since one can have anomalously small eigenvalues of a massive Wilson-Dirac operator that is used as a kernel for the massless overlap Dirac operator. Preliminary investigations suggest that such eigenvalues are suppressed in the continuum limit at a fixed physical volume. Therefore, it should be possible to study the quenched theory with a compact gauge action if one improves the gauge action and the fermion operator used as the probe. A diverging condensate will suggest that monopoles play a physical role in the theory. This will also make it interesting to study QED_3 with dynamical fermions and a compact gauge action.

Acknowledgments

We would like to thank Shai Chester, Igor Klebanov, Max Metlitski, Silviu Pufu, T. Senthil and Cenke Xu for useful discussions during a workshop at the Princeton Center for Theoretical Science. All computations in this paper were made on the JLAB computing clusters under a class C project. The authors acknowledge partial support by the NSF under grant number

PHY-1515446.

---

[1] N. Karthik and R. Narayanan, Phys. Rev. **D93**, 045020 (2016), 1512.02993.

[2] N. Karthik and R. Narayanan, Phys. Rev. **D94**, 065026 (2016), 1606.04109.

[3] S. Hands, J. Kogut, and C. Strouthos, Nucl.Phys. **B645**, 321 (2002), hep-lat/0208030.

[4] W. Rantner and X.-G. Wen, Phys. Rev. Lett. **86**, 3871 (2001), cond-mat/0010378.

[5] W. Rantner and X.-G. Wen, Phys. Rev. **B66**, 144501 (2002).

[6] Y. Huh and P. Strack, JHEP **01**, 147 (2015), [Erratum: JHEP03,054(2016)], 1410.1902.

[7] S. Giombi, G. Tarnopolsky, and I. R. Klebanov, JHEP **08**, 156 (2016), 1602.01076.

[8] S. M. Chester and S. S. Pufu, JHEP **08**, 019 (2016), 1601.03476.

[9] C. Xu and Y.-Z. You, Phys. Rev. **B92**, 220416 (2015), 1510.06032.

[10] A. Karch and D. Tong, Phys. Rev. **X6**, 031043 (2016), 1606.01893.

[11] P.-S. Hsin and N. Seiberg, JHEP **09**, 095 (2016), 1607.07457.

[12] C. Wang, A. Nahum, M. A. Metlitski, C. Xu, and T. Senthil (2017), 1703.02426.

[13] S. Hands and J. B. Kogut, Nucl. Phys. **B335**, 455 (1990).

[14] M. Hermele, T. Senthil, and M. P. A. Fisher, Phys. Rev. **B72**, 104404 (2005), cond-mat/0502215.

[15] S. M. Chester and S. S. Pufu, JHEP **08**, 069 (2016), 1603.05582.

[16] J. J. M. Verbaarschot and I. Zahed, Phys. Rev. Lett. **73**, 2288 (1994), hep-th/9405005.

[17] R. J. Szabo, Nucl. Phys. **B598**, 309 (2001), hep-th/0009237.

[18] M. L. Mehta, Random Matrices, Pure and Applied Mathematices Series **142** (2004).

[19] S. M. Nishigaki, PoS **LATTICE2015**, 057 (2016), 1606.00276.

[20] N. Karthik and R. Narayanan, Phys. Rev. **D94**, 045020 (2016), 1607.03905.

[21] P. H. Damgaard, Nucl. Phys. **B608**, 162 (2001), hep-lat/0105010.

[22] P. H. Damgaard, U. M. Heller, R. Narayanan, and B. Svetitsky, Phys. Rev. **D71**, 114503 (2005), hep-lat/0504012.